Journal of Modern Optics
Publication details, including instructions for authors and subscription information:
http://www.informaworld.com/smpp/title~content=t713191304

Field profiles of coupled surface plasmon-polaritons

Lucy H. Smith [a]; Melita C. Taylor [a]; Ian R. Hooper [a]; William L. Barnes [a]
[a] School of Physics, University of Exeter, Exeter, UK

Online Publication Date: 01 October 2008

To cite this Article Smith, Lucy H., Taylor, Melita C., Hooper, Ian R. and Barnes, William L.(2008)'Field profiles of coupled surface plasmon-polaritons',Journal of Modern Optics,55:18,2929 — 2943
To link to this Article: DOI: 10.1080/09500340802271250
URL: http://dx.doi.org/10.1080/09500340802271250

Journal of Modern Optics
Vol. 55, No. 18, 20 October 2008, 2929–2943

Taylor & Francis
Taylor & Francis Group

Field profiles of coupled surface plasmon-polaritons

Lucy H. Smith[†], Melita C. Taylor, Ian R. Hooper and William L. Barnes*

School of Physics, University of Exeter, Exeter, UK

(*Received 21 April 2008; final version received 2 June 2008*)

We present a study of the electromagnetic field profiles for coupled surface plasmon-polariton systems. Results for both the symmetrically-clad thin metal film structure and the metal-clad dielectric cavity are given. We also consider an asymmetrically-clad thin metal-film structure and show that such a structure may also support coupled SPP modes under appropriate conditions. We describe our method for calculating the field profiles in detail. In contrast to previous methods our approach does not require the introduction of an input field, it allows straightforward computation of the field profiles associated with the optical modes of multilayer planar structures.

Keywords: surface plasmon; guided modes; multilayers; polaritons

1. Introduction

Electric and magnetic field profiles are a powerful tool in analysing the optical response of a multilayer system. A field profile shows how the strength of a particular field component, usually associated with a resonant mode of the structure, changes as a function of distance through the structure. Field profiles can be especially beneficial when looking at guided optical modes, as different types of such modes can have very different field profiles. Field profile information is valuable in deciding where one wishes to place absorbers in thin-film structures, for example photovoltaic cells [1], or where to place emitters, for example in organic light-emitting diodes [2]; it is also important in other types of more fundamental investigation, for example strong coupling [3].

There are two methods commonly used to calculate field profiles. The first is based on a matrix approach, often called the transfer matrix approach. For an outline of the technique see [4]. For a multilayer stack the field components at a position z_1 (z is the direction normal to the planes of the stack) are related to those at a position z_2 by matrices, see Figure 1. In a multilayer structure the overall matrix for the stack is assembled by multiplying together matrices that characterise the individual interfaces and layers. Hence, by starting with a known field incident upon a given structure, the fields throughout the rest of this structure may be calculated. The second method follows that of

*Corresponding author. Email: w.l.barnes@ex.ac.uk
[†]Present address: IOP Publishing, Dirac House, Temple Back, Bristol, UK.

ISSN 0950–0340 print/ISSN 1362–3044 online

DOI: 10.1080/09500340802271250
http://www.informaworld.com

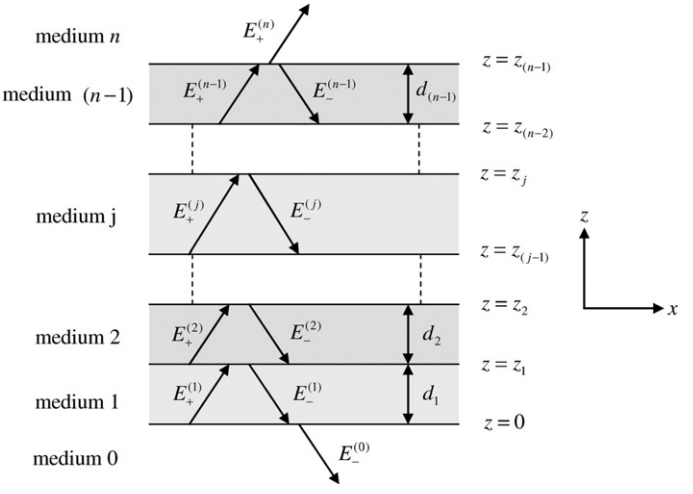

Figure 1. Showing the multilayer structure considered in the field model, indicating the nomenclature used.

Kovacs (see the chapter by Kovacs in [5]) in which an iterative process is used to calculate the fields. Both techniques use the Fresnel reflection and transmission coefficients together with the electromagnetic (EM) boundary conditions at each of the interfaces to find relationships between the field components of adjacent layers.

Both of these approaches are usually implemented in a way that limits their applicability for what we wish to do here, i.e. study guided modes. Specifically, as usually implemented, only field distributions associated with potentially radiative modes may be determined – if one wishes to look at guided modes then structures capable of allowing radiation to couple such modes (e.g. prism couplers) need to be included. If one is interested in looking at the underlying physics then being able to calculate the field profile in the absence of any incident field would be an advantage. More specifically, the inclusion of some kind of input coupler inevitably perturbs the modes that one wishes to study. One can of course make the perturbation smaller and smaller and look at the asymptotic limit, but this is often time consuming. We have modified the second method mentioned above so that no incident field needs to be included in the modelling. Instead, as will be seen below, all that is required is a knowledge of the in-plane wavevector of the mode in question. Since our purpose is to look at field profiles rather than discuss the calculation technique in detail, we omit the details from the main text. However, to provide a clear and single-source version of the relevant equations, details are presented in Appendix 1.

Below, in Section 2, we illustrate the power of this technique by presenting results for various systems which support surface plasmon-polariton (SPP) modes, modes that are of much topical interest [6,7]. We concentrate on coupled SPP modes [8] and display the form of their associated field profiles, including an analysis of the previously little explored coupled modes of asymmetrically-clad thin metal films. Conclusions are drawn in Section 3.

2. Surface plasmon-polariton field profiles

We begin by looking at the surface plasmon-polariton mode supported by a simple system consisting of a metal and a dielectric separated by a planar interface as this helps us to develop a clearer understanding of the SPP modes of more complicated systems. We then move on to study the symmetric dielectric–metal–dielectric thin film and metal–dielectric–metal cavity structures, presenting field profiles in each case. Finally, we consider a metal film bounded on each side by different dielectric materials.

2.1. *Single interface*

Surface plasmon-polaritons are guided electromagnetic (EM) modes that propagate along the interface between a metal and a dielectric [9,10]. They result from coupling between free surface charges at the surface of the metal and EM radiation. This coupling leads to both longitudinal surface charge density oscillations that propagate along the metal–dielectric interface, and to oscillating EM fields that decay in strength exponentially with distance away from the interface.

Let us now consider an example of such a single-interface system, one that comprises silver (Ag) and air. Both the metal and air extend semi-infinitely away from the interface. It is useful at this stage to examine the dispersion relationship for surface plasmon-polaritons on this interface, i.e. to look at how the wavevector of this mode (in the plane of the interface on which they propagate) depends on frequency. A convenient way to do this is by calculating the power dissipated by an oscillating dipole source placed close (50 nm) to the interface using a classical oscillating dipole model [11–14] in which the source is considered to be a forced, damped, harmonic oscillator. Plotting the dissipated power as a function of in-plane wavevector (k_x) (Figure 2(*a*)) reveals peak(s) indicating that power is coupled from the source to the modes associated with the structure: plots such as Figure 2(*a*) are known as power dissipation spectra [12]. The sharp peak in Figure 2(*a*) indicates coupling of the source to the SPP mode associated with the metal–air interface. Whilst the strength of the coupling depends on the position and orientation of the dipole source, the frequency and wavevector of the mode are determined solely by the structure. In all of the simulations reported here the dissipated power has been averaged over all dipole orientations.

By carrying out such calculations for a range of frequencies a dispersion diagram such as Figure 2(*d*) can be built up (the frequency dependent relative permittivity was taken from [15]: the section by Lynch and Huttner) – data being interpolated with the aid of a ninth-order polynomial fit. Here the power dissipated is indicated on a grey scale (dark areas represent significant power coupled from the source and thus indicate the presence of a mode) as a function of frequency and in-plane wavevector. This technique offers a convenient way to identify the different electromagnetic modes that a given structure supports [16], and provides information in a format suitable for comparison with experiment [17]. The dark feature in Figure 2(*d*) represents coupling of the emitter to the SPP mode at the Ag–air interface, the air light-line is also labelled. It should be noted that, as the SPP lies to the right of the light-line, the SPP mode can not radiate into the air, instead it remains bound to the interface. Power dissipation spectra for the symmetric

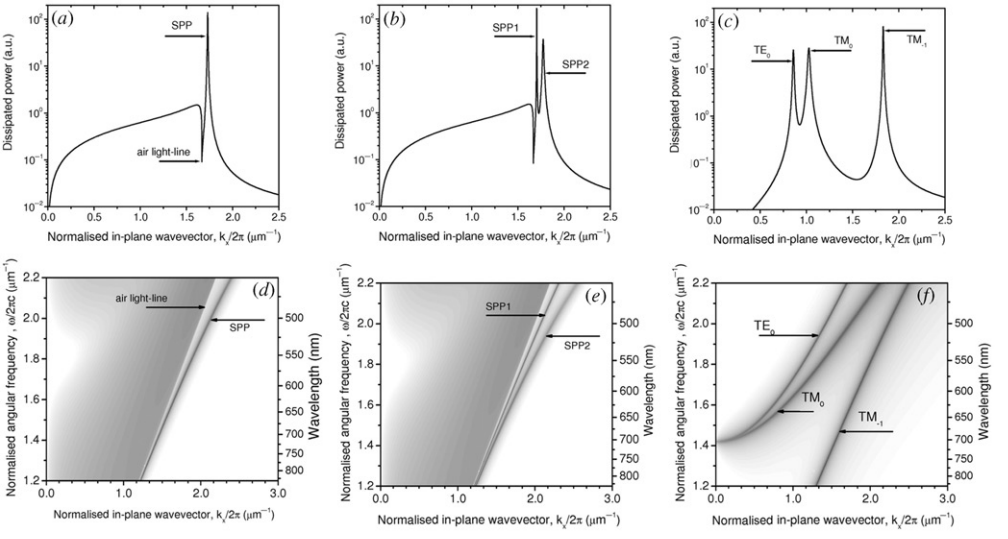

Figure 2. Power dissipation spectra (*a–c*) and dispersion diagrams (*d–f*) for a single metal–air interface (left column), an air–metal–air structure (thin metal film) (centre column) and a metal–air–metal structure (metal-clad cavity) (right column). In the power dissipation spectra the power dissipated by an isotropic emitter is plotted as a function of in-plane wavevector for a dipole 50 nm distant from one of the metal interfaces. For the thin metal film the metal was 50 nm thick, for the metal-clad cavity the cavity (air) was 300 nm thick. For all power dissipation spectra the wavelength was 600 nm and the permittivity of the metal (silver) was taken as $-13.8 + 0.59\mathrm{i}$. For the dispersion diagrams the permittivity of silver was based on a ninth-order polynomial fit to experimental data [15].

structures considered later are also shown in Figure 2 to allow easy comparison between the dispersion diagrams of the different structures.

Taking the power dissipation spectrum (Figure 2(*a*)), one can calculate the in-plane wavevector of the SPP mode at the frequency (wavelength, 600 nm) for which this power dissipation spectrum was calculated, the value is 1.7304 μm^{-1}, where we have normalised the in-plane wavevector as $k_x/2\pi$. This value is then entered into the field profile model (as described above and in Appendix 1) to give the fields associated with the SPP. The time-averaged field components are shown in Figure 3(*a*) and the instantaneous value of the E_z component in Figure 3(*d*). The time-averaged field distributions are calculated using Equation (22) (see Appendix 1). The instantaneous normal field component, E_z, displays the characteristic features of a SPP mode. Firstly, the field is discontinuous at the boundary and changes sign across it. Secondly, the exponential decay of the field occurs far more rapidly in the Ag layer than in the air [18].

By introducing a second metal–dielectric interface into the system there is a possibility that the SPPs associated with each of the separate interfaces may interact to form *coupled* SPPs. There are two ways in which this may be done, either by considering a metal-clad cavity where coupling takes place across the dielectric that separates the two metal surfaces, or a thin-film system where coupling takes place across the metal film. Both are discussed below.

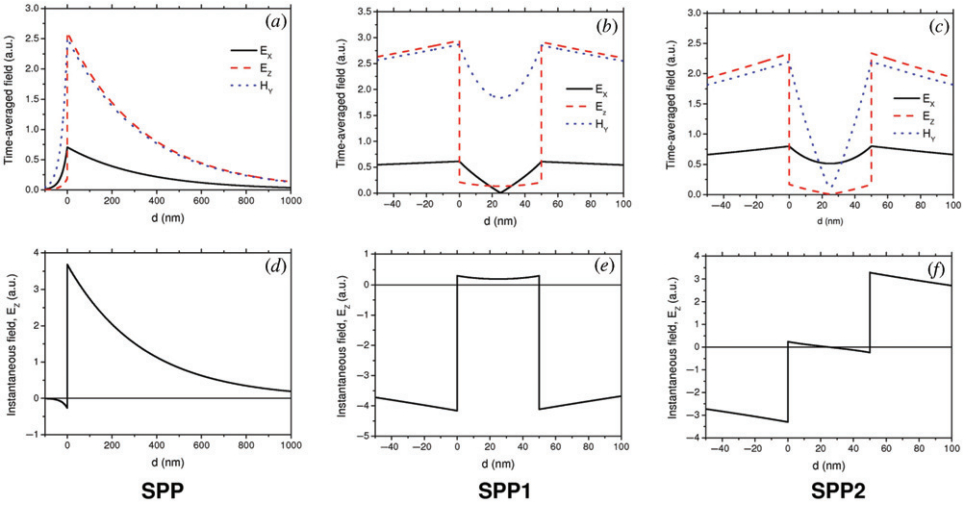

Figure 3. Field distributions for the surface plasmon-polariton (SPP) mode of a single metal–air interface (left column), and the field distributions of the SPP1 and SPP2 modes of the thin metal film (air–metal–air structure) (middle and right columns). The top row shows the time-averaged field components, the lower row the instantaneous value of just one component. For all three simulations the wavelength was 600 nm, and the relative permittivity of the metal (silver) was taken as $-13.8 + 0.59$i. All modes are TM polarised. The in-plane wavevectors correspond to the position of the associated modes in Figures 2(*a*) and (*b*). For the single interface SPP mode the in-plane wavevector is $1.039k_0$, for the thin metal film system SPP1 is calculated at a wavevector of $1.0225k_0$ and SPP2 at $1.0644k_0$. In parts (*b*), (*c*), (*e*) and (*f*), the metal film occupies the region $0\,\text{nm} \leq d \leq 50\,\text{nm}$.

2.2. *Coupled SPPs of dielectric–metal–dielectric structures*

The structure studied here consists of a thin Ag film bounded on both sides by air. A power dissipation spectrum and the dispersion diagram are shown in Figures 2(*b*) and (*e*) for the case of a 50 nm Ag film bounded by air. In Figure 4(*a*) a rather different dispersion is shown – this time rather than varying the frequency for a given film thickness (as shown in Figure 2(*e*)) the frequency is fixed (equivalent to a wavelength of 600 nm) and the thickness of the silver film is varied. It may be seen from Figure 4(*a*) that when the silver is greater than about 80 nm in thickness the two modes, one on each Ag–air interface, are degenerate. As the thickness is decreased these modes interact giving rise to two coupled SPP modes (designated SPP1 and SPP2) – the degeneracy is lifted. The physics here is the same as that found for the way the modes on the inside and outside of a metallic shell may couple and hybridise [19]. As may be seen from Figure 2(*e*), SPP1 lies closer to the light-line than SPP2. This means that SPP1 is more like a photon in character, it corresponds to the lower loss of the two modes. This view is strengthened from an examination of Figure 2(*b*) where we see that SPP1 is the sharper of the two modes. It is often known as the long-range surface plasmon polariton (LRSPP) [20–23].

The charge distributions of the two modes are illustrated in Figure 5, with (*a*) and (*b*) showing the symmetric and antisymmetric charge distributions, respectively. The symmetric case corresponds to SPP2 and the antisymmetric case to SPP1. Note that the assignment of

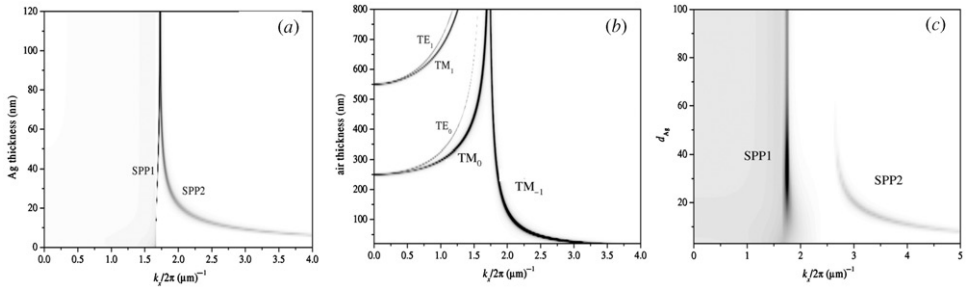

Figure 4. Dispersion diagrams of the surface plasmon-polariton modes associated with (*a*) symmetrically-clad thin metal film (air–silver–air) (left), (*b*) symmetric metal–air–metal cavity (middle) and (*c*) asymmetrically-clad thin metal film (air–silver–glass) (right). Here the wavelength is held fixed at 600 nm and the thickness of the metal film ((*a*) and (*c*)) or air cavity (*b*) is varied. The relative permittivity of the metal (silver) was taken as $-13.8 + 0.59$i.

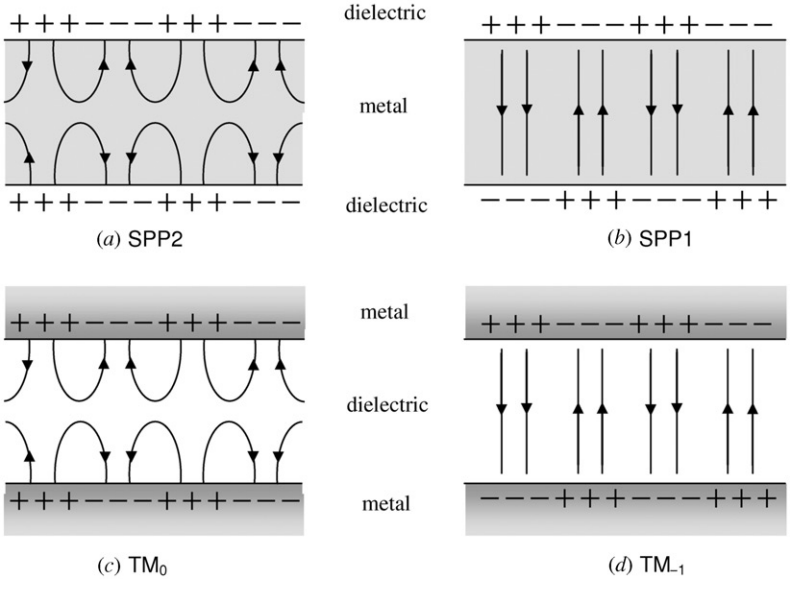

Figure 5. Charge distributions for the modes of a thin metal film (upper) and a metal-clad cavity (lower). Symmetric distributions are shown on the left, asymmetric on the right. (*a*) SPP2; (*b*) SPP1; (*c*) TM_0; (*d*) TM_{-1}.

the asymmetric charge distribution as the SPP1 (long-range) and symmetric as the SPP2 (short-range) is contrary to a previous work [24] – that work was wrong, the error arising from not properly considering all of the field components. For the SPP modes supported by a thin metal film it is the electric field parallel to the interfaces that dominates inside the metal, in judging the relative loss of the modes it is thus important to consider this parallel component – see Figures 3(*b*) and (*c*).

The values of the in-plane wavevector of the peaks associated with the modes in Figure 2(*b*) are used to obtain field profiles, shown in Figures 3(*b*), (*c*), (*e*) and (*f*). For SPP1 the E_z component keeps the same sign throughout the metal film whilst E_x changes sign. In the case of SPP2 these roles are reversed, with E_z passing through zero and E_x remaining the same sign. Integrating under the profiles (with the air regions taken to be much thicker than those illustrated here) reveals that the short-range mode contains a greater fraction of its field within the Ag layer than the long-range mode, confirming the attribution of SPP1 and SPP2 as the long- and short-range surface plasmon-polariton modes, respectively.

2.3. *Coupled SPPs of metal–dielectric–metal structures*

The structure we consider now is an air cavity bounded on both sides by silver. If the air region is very thick, i.e. $\gg \lambda$, then the fields corresponding to the two identical SPP modes on each of the interfaces do not overlap with each other, due to their strength falling off exponentially with distance into the dielectric, the two modes are thus degenerate. However, as the thickness of the cavity is decreased the fields associated with the two modes overlap with each other, the modes interact, and the degeneracy is lifted – a pair of coupled modes are produced, the properties of which can be tailored rather elegantly, for example to show an effective negative index [25,26].

The nature of the modes supported by the cavity structure may be seen in Figure 4(*b*), a dispersion diagram showing the change in dissipated power as a function of the cavity (air) thickness and k_x. This plot is for an emission wavelength of 600 nm. It may be seen that as the cavity thickness is increased the two lowest-order TM modes move closer together. Further results (not shown) indicate that the modes become degenerate for cavity thicknesses above about 1000 nm. The other modes supported are the TE modes and higher order TM waveguide modes, with the number of these modes supported by the cavity rising as the cavity thickness is increased. The mode labelled TM_0 has a cut-off at the same cavity thickness as the TE_0 waveguide mode, whilst the mode labelled TM_{-1} has no cut-off [27].

We now look at a specific cavity thickness of 300 nm. As may be seen from Figure 4(*b*) there are three modes supported by this structure, one TE waveguide mode and a pair of coupled SPP modes. The dispersion of the modes as ω is changed is shown in Figure 2(*f*) with a slice through this plot at 600 nm illustrated in Figure 2(*c*).

The in-plane wavevectors of the peaks associated with the modes are again used to obtain field profiles, Figure 6. The instantaneous E_z component of the TM_{-1} mode does not fall to zero at the centre of the cavity, Figure 6(*f*), suggesting an antisymmetric charge distribution, Figure 5(*d*). The E_z component of the TM_0 mode, by contrast, does pass through zero, the field changing sign through the cavity, Figure 6(*e*). The H_z component of the TE waveguide mode verifies that this is the zeroth order mode – the cavity contains approximately half a wavelength, Figure 6(*d*).

Again, as with the dielectric–metal–dielectric structure, symmetric and antisymmetric refer to the charge distributions on the two metal surfaces with respect to the midpoint of the layer. In the symmetric case, Figure 5(*c*), like-charges are directly opposite and hence act to repel each other when the metal layers are brought closer together. Hence, this charge distribution has a cut-off and corresponds to the TM_0 mode. By contrast, there is

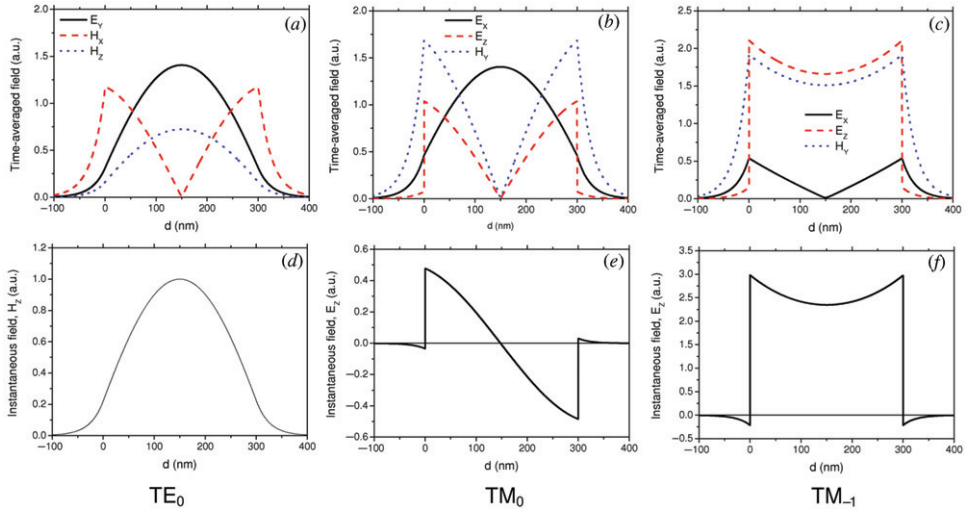

Figure 6. Field profiles of three modes associated with the metal-clad air cavity. Left is the TE_0 mode, centre is the TM_0 mode, right is the TM_{-1} mode. The top row shows the time-averaged field components, the lower row the instantaneous value of just one component. For all three simulations the wavelength was 600 nm, and the relative permittivity of the metal (silver) was taken as $-13.8 + 0.59$i, and the cavity thickness was 300 nm The in-plane wavevectors of the modes, taken from Figure 2(*c*), are for the TE_0 $0.515k_0$, for the TM_0 mode $0.6162k_0$, and for the TM_{-1} mode $1.0992k_0$. In all figures the air cavity occupies the region $0\,\text{nm} \leq d \leq 300\,\text{nm}$.

no cut-off thickness for the antisymmetric charge distribution, Figure 5(*d*), which corresponds to the TM_{-1} mode; this situation is analogous to a parallel plate capacitor.

We can also consider the relative range (propagation distance) of these two modes. We can assign the TM_0 mode and the TM_{-1} mode as the short-range and long-range SPP modes with the assistance of Figure 6. By integrating under the curves we find that the TM_0 has a greater proportion of its fields in the metal than does the TM_{-1}. This means that the TM_0 suffers a greater loss due to damping within the metal layer, hence its propagation length is shorter. This conclusion is reinforced by looking at Figure 2(*c*); the TM_{-1} mode is sharper than the TM_0 mode.

In our final example we consider a thin Ag film bounded on one side by air and on the other by silica (glass). The interest in this system is that it is one frequently encountered in experiments [28]. Surprisingly, as we now show, even though this structure is asymmetrically clad, coupled plasmon modes are still possible.

2.4. *Asymmetric thin metal film*

Figure 4(*c*) illustrates a dispersion diagram with the thickness of the Ag layer changing from 3 to 100 nm, and where we have assumed the dipole source for the calculation to lie in the air 50 nm from the Ag. There are two modes present and these correspond to SPP modes, labelled SPP1 and SPP2. From the dispersion diagram it appears that the two SPP modes adopt a coupled nature when the metal is very thin – apparent from the way

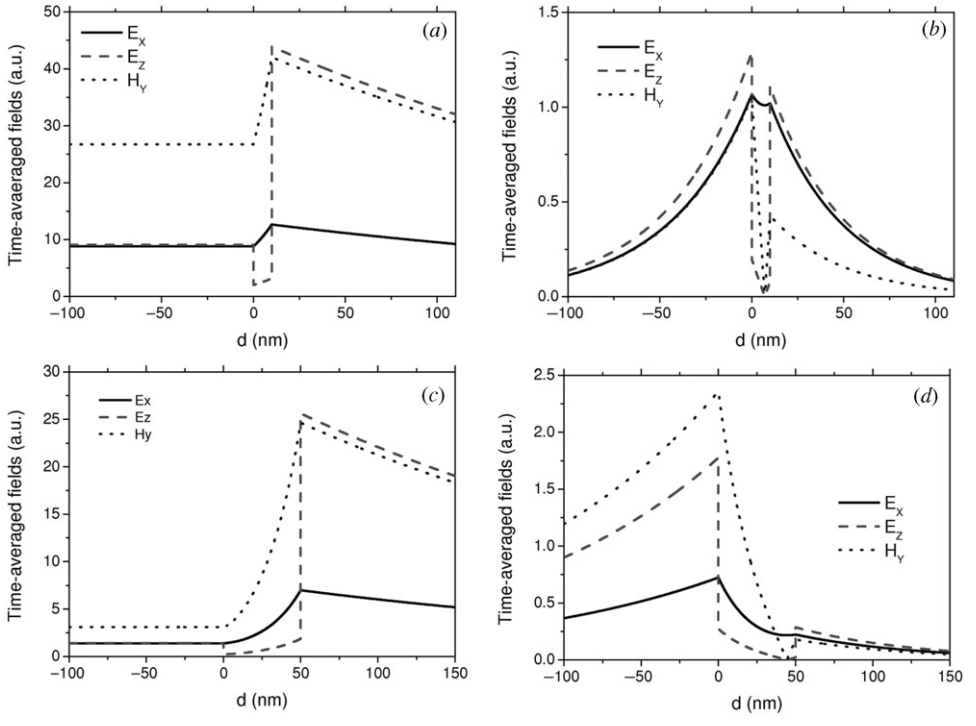

Figure 7. Time-averaged field distributions for the surface plasmon-polariton modes associated with an asymmetrically clad thin metal film. The structure considered is a thin metal (silver) film clad on one side by glass and on the other by air. The top row is for a 10 nm thick silver film, showing the fields for the SPP2 (in-plane wavevector $1.0443k_0$) and SPP1 (in-plane wavevector $2.591k_0$) modes (see Figure 4(*c*)). The bottom row is for a 50 nm thick silver film, showing the fields for the SPP2 (in-plane wavevector $1.03939k_0$) and SPP1 (in-plane wavevector $1.5944k_0$) modes. For all simulations the wavelength was 600 nm, and the relative permittivity of the metal (silver) was taken as $-13.8 + 0.59$i.

SPP2 rapidly increases in-plane wavevector as the metal film thickness is reduced. This may be verified by the use of field profiles.

Figure 7 shows the field profiles for this asymmetric thin film system when the metal has a thickness of 10 nm, data are shown for both the SPP1 and SPP2 modes. It may be seen that the two modes, SPP1 and SPP2, are very different in character, and that due to the asymmetry of the system, the field profiles are asymmetric. Knowing that such asymmetric structures can support coupled surface plasmon-polariton modes is important when one tries to understand the nature of light–matter interactions such as fluorescence [28–30]) and energy transfer [31] when these interactions take place across a metal film.

3. Conclusions

We have outlined a method for calculating the field profiles of electromagnetic modes of planar multilayer structures. The method is based upon that of Kovacs [5], but our modified version avoids the need to impose an input field. The advantage of this

modification is that it allows us to study easily the field distributions of non-radiative modes such as surface plasmon-polaritons. We have demonstrated the use of this model to compute EM field profiles for SPP modes and, by way of example, have presented a comprehensive field-profile analysis of coupled SPP modes. We have also shown that an asymmetric thin film system may support coupled SPP modes.

Acknowledgements

MCT would like to thank the Annual Fund of the University of Exeter for provision of a vacation scholarship. This work was supported in part by the Royal Society through a Wolfson Merit Award (WLB) and in part by the EPSRC. WLB is indebted to Piers Andrew for many discussions on field profiles and it is a pleasure to acknowledge his involvement with the early stages of this work.

References

[1] Peumans, P.; Yakimov, A.; Forrest, S.R. *J. Appl. Phys.* **2003,** *93,* 3693–3723.
[2] Ziebarth, J.M.; McGehee, M.D. *J. Appl. Phys.* **2005,** *97,* 064502-1–7.
[3] Lidzey, D.G.; Bradley, D.D.C.; Skolnick, M.S.; Virgili, E.; Walker, S.; Whittaker, D.M. *Nature* **1998,** *395,* 53–55.
[4] Azzam, R.M.A.; Bashara, N.M. *Ellipsometry and Polarised Light;* Amsterdam: North Holland, 1977.
[5] Boardman, A.D. *Electromagnetic Surface Modes;* Wiley: Chichester, 1982.
[6] Barnes, W.L.; Dereux, A.; Ebbesen, T.W. *Nature* **2003,** *424,* 824–830.
[7] Zayats, A.V.; Smolyaninov, I.I.; Maradudin, A.A. *Phys. Rep.-Rev. Sec. Phys. Lett.* **2005,** *408,* 131–314.
[8] Economou, E.N. *Phys. Rev.* **1969,** *182,* 539–554.
[9] Raether, H. *Surface Plasmons;* Springer-Verlag: Berlin, 1988.
[10] Maier, S.A. *Plasmonics: Fundamentals and Applications;* Springer: Berlin, 2007.
[11] Chance, R.R.; Prock, A.; Silbey, R. *Adv. Chem. Phys.* **1978,** *37,* 1–63.
[12] Ford, G.W.; Weber, W.H. *Phys. Rep.* **1984,** *113,* 195–287.
[13] Barnes, W.L. *J. Mod. Opt.* **1998,** *45,* 661–699.
[14] Wasey, J.A.E.; Barnes, W.L. *J. Mod. Opt.* **2000,** *47,* 725–741.
[15] Lynch, D.W.; Huttner, W.R. In *Handbook of Optical Constants of Solids:* Comments on the Optical Constants of Metals and an Introduction to the Data of Several Metals; Palik, E.D., Ed.; Academic Press: New York, 1985; pp 275–367.
[16] Worthing, P.T.; Amos, R.M.; Barnes, W.L. *Phys. Rev. A* **1999,** *59,* 865–872.
[17] Giannattasio, A.; Wedge, S.; Barnes, W.L. *J. Mod. Opt.* **2006,** *53,* 429–436.
[18] Barnes, W.L. *J. Opt. A: Pure Appl. Opt.* **2006,** *8,* S87–S93.
[19] Prodan, E.; Radloff, C.; Halas, N.J.; Nordlander, P. *Science* **2003,** *302,* 419–422.
[20] Sarid, D. *Phys. Rev. Lett.* **1981,** *47,* 1927–1930.
[21] Yang, F.Z.; Sambles, J.R.; Bradberry, G.W. *Phys. Rev. B* **1991,** *44,* 5855–5872.
[22] Inagaki, T.; Motosuga, M.; Arakawa, E.T.; Goudonnet, J.P. *Phys. Rev. B* **1985,** *32,* 6238–6245.
[23] Barnes, W.L.; Sambles, J.R. *Opt. Commun.* **1986,** *60,* 117–122.
[24] Barnes, W.L. *IEEE J. Light. Tech.* **1999,** *17,* 2170–2182.
[25] Shin, H.; Fan, S. *Phys. Rev. Lett.* **2006,** *96,* 073907-1–4.
[26] Lezec, H.J.; Dionne, J.A.; Atwater, H.A. *Science* **2007,** *316,* 430–432.
[27] Yariv, Y. *Quantum Electronics;* Wiley: Singapore, 1989.
[28] Wedge, S.; Barnes, W.L. *Opt. Exp.* **2004,** *12,* 3673–3685.

[29] Gruhlke, R.W.; Holland, W.R.; Hall, D.G. *Phys. Rev. Lett.* **1986,** *56,* 2838–2841.
[30] Lenac, Z.; Tomas, M.S. *Surf. Sci.* **1989,** *215,* 299–318.
[31] Andrew, P.; Barnes, W.L. *Science* **2004,** *306,* 1002–1005.
[32] Stegeman, G.I. *Appl. Opt.* **1983,** *22,* 2243–2245.
[33] Wasey, J.A.E.; Safonov, A.; Samuel, I.D.W.; Barnes, W.L. *Opt. Commun.* **2000,** *183,* 109–121.
[34] Lorrain, P.; Corson, D.R.; Lorrain, F. *Electromagnetic Fields and Waves;* W.H. Freeman and Company: New York, 1988.

Appendix 1. Calculating field profiles

Here we present a method for calculating field profiles associated with the optical modes of a planar multilayer system. We adapt the method of Kovacs [5], adapted to deal with such modes. The simplest case occurs when the media are isotropic, and we consider this case first, a modification allowing the modelling of uniaxial materials [32] is discussed later, and is useful in birefringent devices such as some organic light-emitting diodes [33].

A schematic of a multilayer system is illustrated in Figure 1 and displays the labelling of the layers and interfaces and shows the direction of propagation of the fields. It should be noted that medium 0 contains only one wave, propagating in the negative z-direction – there is no incident wave. This is in contrast to conventional models in which a wave incident from a glass prism is used to investigate the system. The advantage of the method presented here is that it allows modes with high in-plane wavevector (k_x) values to be probed – such modes are often inaccessible to an incident wave from a prism.

Here, we deal first with isotropic materials, and provide solutions for electric ($\boldsymbol{E}$) and magnetic ($\boldsymbol{H}$) fields for both TM (p-polarised) and TE (s-polarised) modes. Maxwell's equations for non-magnetic media yield the wave equation for the electric field,

$$\nabla^2 \boldsymbol{E} = \frac{\varepsilon}{c}\frac{\partial^2 \boldsymbol{E}}{\partial t^2}. \tag{1}$$

With the propagation of plane waves defined to be in the x–z plane. A solution to Equation (1) is given by

$$\boldsymbol{E} = \boldsymbol{E}\exp[\mathrm{i}(k_x x - \omega t)]\exp(\mathrm{i}k_z z)(x, y, z), \tag{2}$$

where $k_z = [\varepsilon(\omega/c)^2 - k_x^2]^{1/2}$. $\boldsymbol{E}$ is in the direction of the field, ω is the angular frequency of the plane waves, ε is the relative dielectric permittivity, and k_x and k_z are the in-plane and normal wavevector components, respectively, and (x, y, z) defines the direction of the field in terms of Cartesian components. Below, the two polarisations, TM and TE, are dealt with in turn.

TM-polarisation

Waves which are TM-polarised are characterised by the field components E_x, E_z and H_y. The TM modes of a structure containing $(n+1)$ media are described by Equations (3), where an implicit time dependence of $\exp(-\mathrm{i}\omega t)$ has been assumed. An implicit dependence of $\exp(\mathrm{i}k_x x)$ is also assumed since k_x is conserved throughout the system (it is invariant).

$$\begin{aligned}
\boldsymbol{E}^{(0)} &= E_-^{(0)}\exp[-\mathrm{i}k_{0z}(z - z_0)](1, 0, k_x/k_{0z}), \quad z \le 0,\\
\boldsymbol{E}^{(j)} &= E_+^{(j)}\exp[\mathrm{i}k_{jz}(z - z_{j-1})](1, 0, -k_x/k_{jz}),\\
&\quad + E_-^{(j)}\exp[-\mathrm{i}k_{jz}(z - z_j)](1, 0, k_x/k_{jz}), \quad z_{j-1} \le z \le z_j,\\
\boldsymbol{E}^{(n)} &= E_+^{(n)}\exp[\mathrm{i}k_{nz}(z - z_{n-1})](1, 0, -k_x/k_{nz}), \quad z_{n-1} \le z,\\
\boldsymbol{H}^{(0)} &= \frac{\omega}{c}E_-^{(0)}\exp[-\mathrm{i}k_{0z}(z - z_0)](0, -\varepsilon^{(0)}/k_{0z}, 0), \quad z \le 0,
\end{aligned}$$

$$\boldsymbol{H}^{(j)} = \frac{\omega}{c} E_+^{(j)} \exp[\mathrm{i}k_{jz}(z - z_{j-1})](0, \varepsilon^{(j)}/k_{jz}, 0) + \frac{\omega}{c} E_-^{(j)} \exp[-\mathrm{i}k_{jz}(z - z_j)](0, -\varepsilon^{(j)}/k_{jz}, 0), \quad z_{j-1} \le z \le z_j,$$

$$\boldsymbol{H}^{(n)} = \frac{\omega}{c} E_+^{(n)} \exp[\mathrm{i}k_{nz}(z - z_{n-1})](0, \varepsilon^{(n)}/k_{nz}, 0), \quad z_{n-1} \le z, \tag{3}$$

where $k_{jz} = [\varepsilon^{(j)}(\omega/c)^2 - k_x^2]^{1/2}$. The components of $\boldsymbol{H}$ are found using Maxwell's equations in a source free region, which yield $H = Ek/\omega$ (for non-magnetic media) [34]. The subscripts + and- indicate waves travelling in the positive and negative z-directions, respectively, and the superscripts 0, j and n refer to the number of the particular layer in question. The coefficients $E_-^{(0)}, E_+^{(1)}, \ldots, E_+^{(n)}$ are amplitude coefficients. We set the x-component of the electric field amplitude to unity; this also means that for s-polarised waves the y-component of the electric field amplitude is unity. It should be noted that the $\boldsymbol{H}$ fields have been multiplied by a factor of c to make them comparable in size to the $\boldsymbol{E}$ fields, this makes numerical computation easier.

To calculate the field profiles, the values of the amplitude coefficients must be determined. This may be done using an iterative technique with the coefficients calculated in terms of one specific coefficient whose value is arbitrary and may be chosen. We take this coefficient to be $E_+^{(1)}$ which we set equal to 1. The iterations begin at the nth boundary, where $z = z_{n-1}$. The boundary conditions require that the tangential components of $\boldsymbol{E}$ and $\boldsymbol{H}$ be continuous across the interfaces. Using these conditions and performing some algebraic manipulation yields both $E_+^{(n)}$ and $E_-^{(n-1)}$ in terms of $E_+^{(n-1)}$,

$$E_+^{(n)} = t_{n-1,n} \exp[\mathrm{i}k_{n-1,z}d_{n-1}]E_+^{(n-1)}, \tag{4}$$

$$E_-^{(n-1)} = r_{n-1,n} \exp[\mathrm{i}k_{n-1,z}d_{n-1}]E_+^{(n-1)}, \tag{5}$$

where t and r represent transmission and reflection amplitude coefficients, respectively, and are given by

$$t_{n-1,n} = \frac{2\varepsilon_{n-1}k_{n,z}}{\varepsilon_{n-1}k_{n,z} + \varepsilon_n k_{n-1,z}}, \tag{6}$$

$$r_{n-1,n} = \frac{\varepsilon_{n-1}k_{n,z} - \varepsilon_n k_{n-1,z}}{\varepsilon_{n-1}k_{n,z} + \varepsilon_n k_{n-1,z}}. \tag{7}$$

By using the boundary conditions, stating that E_x and H_y are continuous across the interfaces, the coefficients associated with each of the layers down to and including layer 1 may be computed. At the interface $z = z_{n-2}$, the coefficients $E_+^{(n-1)}$ and $E_-^{(n-2)}$ are found, in terms of $E_+^{(n-2)}$, to be

$$E_+^{(n-1)} = \frac{t_{n-2,n-1} \exp[\mathrm{i}k_{n-2,z}d_{n-2}]E_+^{(n-2)}}{1 + r_{n-2,n-1}r_{n-1,n} \exp[2\mathrm{i}k_{n-1,z}d_{n-1}]} \tag{8}$$

and

$$E_-^{(n-2)} = r_{n-2,n} \exp[\mathrm{i}k_{n-2,z}d_{n-2}]E_+^{(n-2)}, \tag{9}$$

where $t_{n-2,n-1}$, $r_{n-2,n-1}$ and $r_{n-1,n}$ are defined by Equations (6) and (7). The term $r_{n-2,n}$ is a more complicated reflection term taking account of fields reflected from interface $z = z_{n-1}$ which make their way back through interface $z = z_{n-2}$. This is given by

$$r_{n-2,n} = \frac{r_{n-2,n-1} + r_{n-1,n} \exp[2\mathrm{i}k_{n-1,z}d_{n-1}]}{1 + r_{n-2,n-1}r_{n-1,n} \exp[2\mathrm{i}k_{n-1,z}d_{n-1}]}. \tag{10}$$

This same procedure is carried out at the interface $z = z_{n-3}$ and so on until interface $z = z_1$, where the following relations apply,

$$E_-^{(1)} = r_{1,n} \exp[\mathrm{i}k_{1,z}d_1]E_+^{(1)} \tag{11}$$

and

$$E_+^{(2)} = \frac{E_+^{(1)} t_{1,2}}{1 + r_{1,2} r_{2,n} \exp[2\mathrm{i} k_{1,z} d_1]}, \tag{12}$$

where t_{12} is defined by Equation (6). The coefficients r_{2n} and r_{1n} are defined as follows,

$$r_{2,n} = \frac{r_{2,3} + r_{3,n} \exp[2\mathrm{i} k_{3,z} d_3]}{1 + r_{2,3} r_{3,n} \exp[2\mathrm{i} k_{3,z} d_3]}, \tag{13}$$

$$r_{1,n} = \frac{r_{1,2} + r_{2,n} \exp[2\mathrm{i} k_{2,z} d_2]}{1 + r_{1,2} r_{2,n} \exp[2\mathrm{i} k_{2,z} d_2]}. \tag{14}$$

If all of the layers have a known relative dielectric permittivity then it is possible to calculate all of the reflection and transmission coefficients [Equations (6) and (7)] from r_{01} and t_{01} up to $r_{n-1,n}$ and $t_{n-1,n}$. These reflection coefficients may then be used to calculate all of the more complex reflection terms [e.g. in Equations (10)] from $r_{n-1,n}$ to r_{0n}.

The next step is to deal with the first interface of the system, $z = z_0$. This is where the method used here deviates from that of Kovacs [5], as there is no incident field at this boundary. This leads to a different result for the field amplitude coefficient $E_-^{(0)}$ when the boundary conditions are applied. Some algebraic manipulation gives $E_-^{(0)}$ terms of $E_+^{(1)}$. Equation (15) holds for field components E_x and E_z, with Equation (16) applicable to component H_y.

$$E_-^{(0)} = [r_{1,n} \exp(2\mathrm{i} k_{1,z} d_1) + 1] E_+^{(1)}, \quad \text{for } E_x, E_z, \tag{15}$$

$$E_-^{(0)} = \frac{\varepsilon_1 k_{0,z}}{\varepsilon_0 k_{1,z}} [r_{1,n} \exp(2\mathrm{i} k_{1,z} d_1) - 1] E_+^{(1)}, \quad \text{for } H_y. \tag{16}$$

It is now possible to compute all of the field amplitude coefficients in terms of $E_+^{(1)}$. For simplicity, $E_+^{(1)}$ is set to unity and an iterative process is used to calculate the coefficients in turn. Once these have been established they may be substituted into Equations (3) to give full field solutions for TM-polarised waves.

TE-polarisation

Waves which are TE-polarised are characterised by the field components E_y, H_x and H_z. As for the TM case, the common harmonic factor of $\exp[\mathrm{i}(k_x x - \omega t)]$ has been omitted and the fields for the media are given by:

$$\begin{aligned}
\boldsymbol{E}^{(0)} &= E_-^{(0)} \exp[-\mathrm{i} k_{0z}(z - z_0)](0, 1, 0), \quad z \le 0, \\
\boldsymbol{E}^{(j)} &= E_+^{(j)} \exp[\mathrm{i} k_{jz}(z - z_{j-1})](0, 1, 0), \\
&\quad + E_-^{(j)} \exp[-\mathrm{i} k_{jz}(z - z_j)](0, 1, 0), \quad z_{j-1} \le z \le z_j, \\
\boldsymbol{E}^{(n)} &= E_+^{(n)} \exp[\mathrm{i} k_{nz}(z - z_{n-1})](0, 1, 0), \quad z_{n-1} \le z, \\
\boldsymbol{H}^{(0)} &= \frac{c}{\omega} E_-^{(0)} \exp[-\mathrm{i} k_{0z}(z - z_0)](k_{0z}, 0, k_x), \quad z \le 0, \\
\boldsymbol{H}^{(j)} &= \frac{c}{\omega} E_+^{(j)} \exp[\mathrm{i} k_{jz}(z - z_{j-1})](-k_{jz}, 0, k_x), \\
&\quad + \frac{c}{\omega} E_-^{(j)} \exp[-\mathrm{i} k_{jz}(z - z_j)](k_{jz}, 0, k_x) \quad z_{j-1} \le z \le z_j, \\
\boldsymbol{H}^{(n)} &= \frac{c}{\omega} E_+^{(n)} \exp[\mathrm{i} k_{nz}(z - z_{n-1})](-k_{nz}, 0, k_x), \quad z_{n-1} \le z,
\end{aligned} \tag{17}$$

where, as for the TM case, $k_{jz} = [\varepsilon^{(j)}(\omega/c)^2 - k_x^2]^{1/2}$, and the $\boldsymbol{H}$ fields have been multiplied by a factor of c.

By applying the boundary conditions – that E_y and H_x are continuous across the interfaces – the relationships between the field amplitude coefficients, for interfaces $2 \ldots (n-1)$, are found to be identical to those for TM-polarisation, but with the reflection and transmission coefficients written as

$$t_{n-1,n} = \frac{2k_{n-1}}{k_{n-1} + k_n}, \tag{18}$$

$$r_{n-1,n} = \frac{k_{n-1} - k_n}{k_{n-1} + k_n}. \tag{19}$$

The field amplitudes for the first layer are given in terms of $E_+^{(1)}$ by

$$E_-^{(0)} = E_+^{(1)}\left[r_{1,n}\exp\left(2ik_{1,z}d_1\right) + 1\right], \quad \text{for } E_y, H_z, \tag{20}$$

$$E_-^{(0)} = E_+^{(1)}\frac{k_1}{k_0}\left[r_{1,n}\exp\left(2ik_{1,z}d_1\right) - 1\right], \quad \text{for } H_x. \tag{21}$$

Substituting the coefficients into Equations (17) gives complete field solutions for TE-polarised waves.

The field solutions for both TM- and TE-polarised waves are in complex form. By separating these into real and imaginary parts the fields at an instant in time may be obtained, with the imaginary component $\pi/2$ ahead in phase of the real component. An average value of the fields over time, known as time-averaged fields, $|F|$, may be calculated by

$$|F| = \left(\frac{1}{2}\right)^{1/2}\left[\Re(F)^2 + \Im(F)^2\right], \tag{22}$$

where F represents the desired field component, and $\Re$ and $\Im$ indicate real and imaginary components, respectively.

Finally, for completeness, we indicate how this formalism may be extended to include layers that are optically uniaxial.

Modelling uniaxial materials

Uniaxial materials have the same permittivity in the x- and y-directions ($\varepsilon_\parallel$), but a different permittivity in the z-direction ($\varepsilon_\perp$). The inclusion of uniaxial materials into the theory can be accomplished by considering the transmission and reflection coefficients, which were defined for isotropic media in Equations (6) and (7), respectively, for TM-polarisation and in Equations (18) and (19), respectively, for TE-polarisation. For a uniaxial medium, TE-polarised light will experience no change in permittivity, so no adaptations are necessary and Equations (18) and (19) still hold. However, TM-polarised light will be affected by the two different permittivities. The modified transmission and reflection coefficients are

$$t_{n-1,n} = \frac{2\varepsilon_{\parallel,n}k_{n-1,z}}{\varepsilon_{\parallel,n-1}k_{n,z} + \varepsilon_{\parallel,n}k_{n-1,z}}, \tag{23}$$

$$r_{n-1,n} = \frac{\varepsilon_{\parallel,n-1}k_{z,n} - \varepsilon_{\parallel,n}k_{z,n-1}}{\varepsilon_{\parallel,n-1}k_{z,n} + \varepsilon_{\parallel,n}k_{z,n-1}}, \tag{24}$$

where

$$k_{z,j} = \left\{ \varepsilon_{\|,j} \left[\left(\frac{\omega}{c} \right)^2 - \left(\frac{k_x^2}{\varepsilon_{\perp,j}} \right) \right] \right\}^{1/2},$$

and n, $n-1$, and j refer to layers of the structure.

Substituting these transmission and reflection coefficients [Equations (23) and (24)] into the equations defined for isotropic materials yields full field solutions for uniaxial media.